

Particle Deposition Driven by Evaporation in Membrane Pores and Droplets

Juliet Jiang, Ruohan Zhang, Dominic Jeong [†]

Project advisor: Thomas Witelski[‡] Graduate Student project manager: Yuqing Dai[§]

Abstract. This paper investigates particle deposition driven by fluid evaporation in a single pore channel representative of those found in porous membranes. A moving boundary problem for the 2D heat equation is coupled with an evolution equation for the pore radius, and describes the physical processes of fluid evaporation, diffusion of the particle concentration, and deposition on the pore channel wall. Furthermore, a stochastic differential equation (SDE) approach based on a Brownian motion particle-level description of diffusion is used as a similar phenomenological representation to the partial differential equation (PDE) model. Sensitivity analysis reveals trends in dominant model parameters such as evaporation rate, deposition rate, the volume scaling coefficient, and investigates the monotonicity of concentration. Evaluations of the asymptotically reduced model and the SDE model against the 2D PDE model are done in terms of the pore radius and solute concentration over time. For further exploration, we apply the model to a 2D droplet as well with both deterministic and stochastic approaches.

Key words. diffusion, evaporation, particle deposition, stochastic differential equations, partial differential equations, moving boundary problem

1. Introduction. When fluid in an open container evaporates, any non-volatile impurities will eventually deposit as residue on the walls of the container. Evaporation of the solvent increases particle concentration until a saturation point is reached, where particles then exit the solution and adhere to the internal walls. The process leaves a distribution of particle mass on dried portions of the container. This phenomenon exists in porous media, which can be described as numerous layers of thin filter membranes composed of microscopic pores, where invasion of a volatile liquid occurs. The evaporation of the impure fluid leads to accumulation of deposited particles such as dirt and dust inside the pore structure. The accumulation of these particles has the potential to cause clogging within the pores, leading to contamination and overall degradation of the material. The problem is well worth investigating as different types of porous media appear in deep filtration and fluid transport problems, occurring naturally from extracellular space to industrial material structure [2, 6]. Pore structure, transport processes, and contaminant deposition all influence the solvent evaporation rate [14]. Thus, given the interplay of these processes, understanding the behavior and patterns of particle deposition and solvent evaporation can provide helpful information for industrial and medical fields to limit contamination and prevent clogging through improved material design.

Existing models have investigated the evaporation process from different perspectives and fields, including factors such as medium properties, internal transport processes, pore geometry, and pore wettability [8, 10]. For this article, the model presented follows along the lines of those presented in a series of annual workshops on Mathematical Problems in Industry

[†]Department of Mathematics, Duke University (dominic.jeong@duke.edu, juliet.jiang@duke.edu, ruohan.zhang690@duke.edu)

[‡]Department of Mathematics, Duke University (witelski@math.duke.edu)

[§]Department of Mathematics, Duke University (ydai39@math.duke.edu)

39 (MPI) in 2020 and 2021, where several industrial representatives from W. L. Gore & As-
40 sociates presented the problem of contamination in porous media or filters. In their work,
41 researchers developed a model that describes evaporation and deposition in a single cylin-
42 drical pore structure [1], examined the effect of physical parameters such as pore length and
43 fluid wetting properties, and observed the response of particle mass distribution to cycles of
44 wetting and drying [14]. This paper makes use of similar important physical phenomena such
45 as evaporation, deposition, and key model attributes (pore radius, fluid concentration).

46 However, the MPI solutions require a limiting case where pores have small aspect ratios
47 (i.e. they are long and narrow). This study considers the model for two-dimensional (2D)
48 domains (with finite aspect ratios) with two moving boundaries, eliminating those geometric
49 assumptions. Additionally, finite difference methods used on irregular boundaries can have
50 lower accuracy due to limited spatial resolution, causing mass to leak from the system. To
51 prevent the loss of mass, rather than having irregular domains shrink as boundaries move,
52 we instead implement fixed computational domains through a change of variables. Moreover,
53 this paper uses stochastic differential equations (SDEs) to model particle behavior in the bulk
54 through tracking individual particle trajectories rather than the fluid body as a whole. The
55 use of SDEs requires the formulation of boundary conditions at the edges of the pore channel
56 and at the fluid-air interface. SDE boundary conditions are still being studied or are very
57 complicated [9], so we are interested in creating SDE boundary conditions that are simpler
58 and easier to manipulate. If the SDE and PDE models show phenomenological similarity, we
59 will have shown the two approaches can describe evaporation and deposition processes in a
60 micro-scale pore.

61 Other scenarios possessing evaporation-deposition interactions include the case where fluid
62 no longer spans the entirety of an open pore channel after evaporation. Surface tension
63 causes the remaining fluid to adhere to side walls as droplets. Droplets along a pore channel
64 are analogous to liquid spills leaving particle-laden drops on a horizontal surface. Further
65 evaporation of fluid in these cases typically results in particles dispersing and leaving unique
66 deposition patterns around the perimeter of the droplet or spill. The mechanism behind
67 development of these ring-like deposits is commonly attributed to the coffee ring effect, and
68 the phenomenon can be detrimental in materials that require uniform deposition [16]. It has
69 been shown that the coffee ring effect originates from outward capillary flow and the droplet's
70 surface tension [7]. However, even without these conditions, understanding deposition patterns
71 through constructing mathematical models can be helpful for many applications. Thus, to
72 conduct a more comprehensive study of particle evaporation and deposition behavior, it is
73 also important to investigate how these droplets evolve.

74 The outline of this paper begins with the construction of the 2D PDE model, detailed from
75 solving the dimensional problem to constructing the non-dimensional model on the computa-
76 tional domain. The subsequent section describes the SDE model with a proposed stochastic
77 algorithm and boundary conditions. Next, an asymptotically reduced 1D model is derived
78 from the 2D model. Results are presented by visual comparison and numerical metrics such
79 as mass and pore radius or concentration evolution, and are followed by a systematic summary
80 of parameter analyses. Lastly, we apply similar computational methods and PDE vs. SDE
81 comparisons to a model of an evaporating droplet.

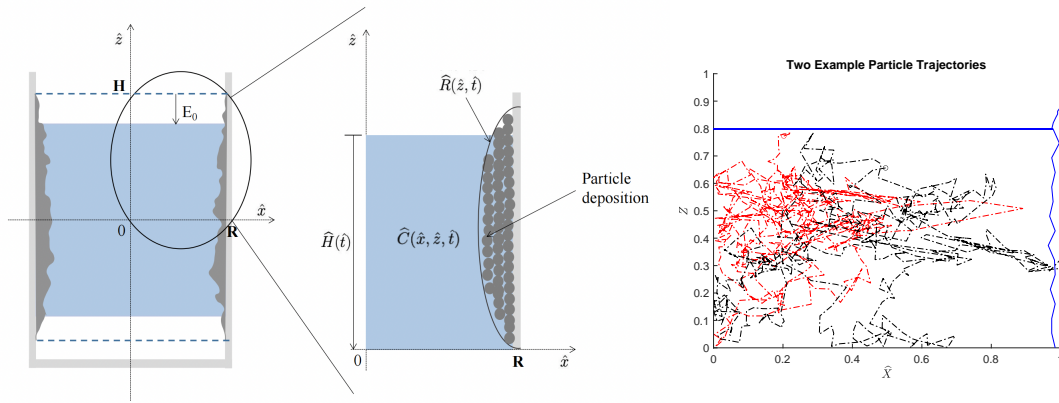


Figure 1: **Left:** Schematic of the reduction from the physical pore to the 2D quarter section described in the PDE model. H and R describe the initial state of the physical pore channel, whereas $\hat{R}(\hat{z}, \hat{t})$ and $\hat{H}(\hat{t})$ represent the evolving dimensions of the pore in the mathematical model. $\hat{C}(\hat{x}, \hat{z}, \hat{t})$ describes concentration in the particle-laden fluid, and E_0 , the evaporation rate, lowers the fluid height. Circular particles illustrate mass accumulation along the right wall. **Right:** Two example particle trajectories in the fluid of the SDE model. Particles move randomly and are contained in the fluid. If adsorption occurs at the wall, accumulation causes the pore radius to narrow.

82 **2. Model Formulation.** In this section, investigation of the reduced 2D model for a single
 83 pore filled with fluid is conducted. As shown in Figure 1 (left), the rectangular pore is sectioned
 84 into symmetrical quarters from the horizontal and vertical center. In the vertical direction,
 85 evaporation takes place at the upper and lower fluid-air interfaces. As evaporation occurs,
 86 fluid height decreases and particles in the fluid, represented in Figure 1 (left) in gray, are
 87 continuously deposited along the internal pore surface in the wet portions of the channel. In
 88 the dry portions of the pore, particles remain on the wall, forming a fixed distribution mass
 89 as the interface lowers. In the horizontal direction, the radius of the pore channel narrows
 90 over time due to particle accumulation on the internal wall. Therefore, the presented problem
 91 consists of two types of moving boundaries: the uniform air-fluid evaporation interface and the
 92 nonuniform, shrinking radius for the fluid-solid deposition interface. Instead of the physical
 93 meniscus shape, we assume the fluid-air interface to be flat and independent of the horizontal
 94 position \hat{x} . The fluid-air interface lowers according to a constant evaporation rate, denoted
 95 by E_0 .

96 Figure 1 (left) also shows that the model in this paper only examines the top-right section
 97 of the channel. The complete behavior of the rectangular pore with suspended liquid can be
 98 inferred from the quarter section. Gravity is neglected in the model to achieve this vertical
 99 symmetry between the upper and lower part of the fluid. The 2D diffusion equation is used to
 100 model the concentration of particles in the fluid body, and is coupled with a PDE describing
 101 the radius of the pore channel. The solvent evaporation rate, particle deposition rate, fluid
 102 initial concentration, and the diffusion of the concentration all contribute to the shape of the

103 accumulating wall, and thus we closely investigate the effect of these properties in our model.

104 Furthermore, since the random motion of particles in the fluid is given by Brownian
 105 motion, it is of interest to see how an SDE model may perform alongside the PDE model,
 106 further described in [section 3](#). Concentration can likewise be defined as a probability density
 107 function of individual particle trajectories [11]. By computationally tracking each particle
 108 trajectory over time as shown in [Figure 1](#) (right), the SDE model defines concentration as
 109 the proportion of particles present in a given area to determine levels of saturation at the
 110 pore wall, from which the probability of local deposition is evaluated. The SDE model gives a
 111 micro-particle approach rather than illustrating macroscopic behavior. However, it is expected
 112 to demonstrate a good agreement of behavior with the PDE model.

113 The initial pore radius is denoted as \mathbf{R} , and the initial height of the fluid surface to the
 114 vertical center of the pore is \mathbf{H} as shown in [Figure 1](#) (left). This model assumes the dilute case;
 115 therefore, the pore channel is initially completely filled with fluid of low particle concentration.
 116 The particle concentration is also uniform across the entire fluid body. Adsorption will occur
 117 on the wall of the channel when local concentration near the boundary exceeds the saturation
 118 concentration defined in the model. The adsorption process is also irreversible, meaning
 119 once the particles deposit onto the wall, they do not re-enter the fluid. For computational
 120 purposes, we ignore the thermodynamic effects to the model including the effect of phase
 121 changes, temperature variations, or humidity variations. Lastly, we also neglect the net drift
 122 velocity of particles in the fluid.

123 **2.1. 2D PDE problem.** As shown in [Figure 1](#), a single 2D pore channel is sectioned with
 124 $\hat{z} = 0$ and $\hat{x} = 0$ being planes of symmetry horizontally and vertically. A system of partial
 125 differential equations is used to model the quarter section of the pore where $\hat{z} \geq 0$ and $\hat{x} \geq 0$,
 126 and \hat{t} as the time variable. With the assumptions above and for $\hat{t} \geq 0$, $\hat{H}(\hat{t})$ is used to denote
 127 the height of the top flat surface from the axis $\hat{x} = 0$. The radius of the pore is represented
 128 by

$$129 \quad (2.1) \quad \hat{R}_{full}(\hat{z}, \hat{t}) = \begin{cases} \hat{R}_{dry}(\hat{z}) & \hat{H}(\hat{t}) < \hat{z} \leq \mathbf{H}, \\ \hat{R}_{wet}(\hat{z}, \hat{t}) & 0 \leq \hat{z} \leq \hat{H}(\hat{t}). \end{cases}$$

130 The region $\hat{H}(\hat{t}) < \hat{z} \leq \mathbf{H}$, above the fluid, is considered as the 'dry' region where the radius
 131 does not further evolve, and we define $\hat{R}_{dry}(\hat{H}(\hat{t})) := \hat{R}_{wet}(\hat{H}(\hat{t}), \hat{t})$ at each time by continuity
 132 at the interface. For the rest of the paper, the model will focus on $\hat{R}_{wet}(\hat{z}, \hat{t})$, simply referred
 133 to as $\hat{R}(\hat{z}, \hat{t})$. To denote the fluid concentration, we use

$$134 \quad (2.2) \quad \hat{C}(\hat{x}, \hat{z}, \hat{t}) \quad \text{defined on the evolving domain} \quad \begin{cases} 0 \leq \hat{x} \leq \hat{R}(\hat{z}, \hat{t}), \\ 0 \leq \hat{z} \leq \hat{H}(\hat{t}). \end{cases}$$

135 The particle concentration in the pore channel is modeled by the diffusion equation, given by
 136

$$137 \quad (2.3) \quad \frac{\partial \hat{C}}{\partial \hat{t}} = D \left(\frac{\partial^2 \hat{C}}{\partial \hat{x}^2} + \frac{\partial^2 \hat{C}}{\partial \hat{z}^2} \right),$$

138 where D is the diffusion constant. Since the model works upon a quarter section of the entire
 139 pore channel, the left and bottom boundaries are the planes of symmetry of the fluid body.
 140 Thus, they are treated as reflecting boundaries, or Neumann symmetry boundary conditions,
 141 written as

$$142 \quad (2.4) \quad \frac{\partial \hat{C}}{\partial \hat{z}} \Big|_{\hat{z}=0} = 0, \quad \frac{\partial \hat{C}}{\partial \hat{x}} \Big|_{\hat{x}=0} = 0.$$

143 The height of the fluid decreases due to evaporation, rendering the top surface, $\hat{z} = \hat{H}$, a
 144 moving boundary. The decreasing height is determined by the constant evaporation rate

$$145 \quad (2.5) \quad \frac{d\hat{H}}{dt} = -E_0,$$

146 and the corresponding no-flux condition at the moving boundary is

$$147 \quad (2.6) \quad \left(-\hat{C} \frac{\partial \hat{H}}{\partial t} - D \frac{\partial \hat{C}}{\partial \hat{z}} \right) \Big|_{\hat{z}=\hat{H}(t)} = 0.$$

148 Additionally, while fluid evaporates, deposition occurs when local concentration near the wall
 149 exceeds a defined saturation concentration C_{sat} . The resulting precipitation flux is defined by
 150 $\hat{Q}(\hat{C})$ where

$$151 \quad (2.7) \quad \hat{Q}(\hat{C}) = \lambda \max(\hat{C} - C_{sat}, 0),$$

152 with $\lambda > 0$ as a dimensional deposition rate. Since deposition happens gradually at the right
 153 wall as time goes by, this side wall is also a moving boundary and could be represented by
 154 the surface $\hat{x} = \hat{R}(\hat{z}, \hat{t})$. The moving boundary condition describing a narrowing pore radius
 155 is then represented through a Robin boundary condition as

$$156 \quad (2.8) \quad \left(-\hat{C} \frac{\partial \hat{R}}{\partial t} - D \frac{\partial \hat{C}}{\partial \hat{x}} + D \frac{\partial \hat{C}}{\partial \hat{z}} \frac{\partial \hat{R}}{\partial \hat{z}} - \hat{Q}(\hat{C}) \sqrt{1 + \hat{R}_z^2} \right) \Big|_{\hat{x}=\hat{R}(\hat{z}, \hat{t})} = 0,$$

157 where the right boundary condition contains a flux term built upon $\hat{Q}(\hat{C})$. Flux exiting the
 158 fluid body yields particles accumulating on the wall and narrowing the pore radius. Thus, the
 159 inward-moving wall can be described as

$$160 \quad (2.9) \quad \frac{\partial \hat{R}}{\partial t} = -\chi \hat{Q}(\hat{C}) \sqrt{1 + \hat{R}_z^2}, \quad \hat{z} \in [0, \hat{H}(\hat{t})],$$

161 where $\chi > 0$ is a dimensional volume scaling coefficient [14]. We use χ to describe the
 162 compression of particles when exiting the solvent and adhering to the wall.

163 To derive the boundary conditions for Equations (2.6) and (2.8), we apply the Leibniz
 164 integral rule to a general expression for the rate of change of mass. The derivation is detailed
 165 in Appendix A. Equation (A.5), a general moving boundary condition with flux, is applied
 166 to: (i) the surface $\hat{x} = \hat{R}(\hat{z}, \hat{t})$ at the wall with prescribed flux of particles Q and (ii) the

Table 1: Table of Dimensional Parameters. Values displayed comprise an example set of parameters taken from [14]. The volume scaling coefficient is set to 0.8 as a conversion factor between fluid concentration and the corresponding deposited volumes on the pore wall, and the saturation concentration is chosen as 0.5 M as per [4]. These values may represent generic reference scales that are physically plausible, or re-scaled through non-dimensionalization, as discussed in Section 2.1.1.

Parameter	Symbol	Value
Evaporation rate (mm/h)	E_0	0.5
Diffusion rate (mm^2/h)	D	1
Precipitation rate coefficient (mm/h)	λ	1
Volume scaling coefficient	χ	0.8
Saturation concentration (mol/L)	C_{sat}	0.5

167 evaporating surface $\hat{z} = \hat{H}(\hat{t})$ with no flux to obtain the two Robin boundary conditions in
 168 this section. Additionally, the initial conditions at $\hat{t} = 0$ of the system of PDE describing the
 169 pore channel is denoted as

(2.10)

$$170 \quad \hat{H}(0) = \mathbf{H}, \quad \hat{R}(\hat{z}, 0) = \mathbf{R} \quad \text{on } 0 \leq \hat{z} \leq \mathbf{H}, \quad \hat{C}(\hat{x}, \hat{z}, 0) = \mathbf{C}_0 \quad \text{on } \begin{cases} 0 \leq \hat{x} \leq \mathbf{R}, \\ 0 \leq \hat{z} \leq \mathbf{H}. \end{cases}$$

171 Example choices of the constant parameters used in the PDE system are defined in Table 1.
 172 With the above initial condition, (2.5) can be solved to give the height as

$$173 \quad (2.11) \quad \hat{H}(\hat{t}) = \mathbf{H} - E_0 \hat{t}.$$

174 Then the ultimate ending time equals $\hat{t}_{end} = \mathbf{H}/E_0$, where $\hat{H}(\hat{t}_{end}) = 0$ and the model stops
 175 as the fluid is completely evaporated. However, the model assumes dilute regimes and the
 176 concentration \hat{C} diverges to infinity as time approaches \hat{t}_{end} and as the solvent evaporates.
 177 Thus, we will stop simulations before reaching \hat{t}_{end} , before the concentration becomes too
 178 high.

179 **2.1.1. Non-dimensionalization.** In order to have a better understanding of the model's
 180 intrinsic behavior, non-dimensionalization is applied to the 2D model with equations (2.3)-
 181 (2.8) so the influence of parameters does not depend on dimensional values. The results in this
 182 section are also implemented in the droplet model discussed in a further section. To conduct
 183 non-dimensionalization, the variables are re-scaled such that

$$184 \quad \tilde{x} = \hat{x}/\mathbf{R}, \quad \hat{x} \in [0, \hat{R}(\hat{z}, \hat{t})] \quad \tilde{z} = \hat{z}/\mathbf{H}, \quad \hat{z} \in [0, \hat{H}(\hat{t})].$$

185 For further convenience, the timescale T is chosen to be dependent on the rate of diffusion
 186 and the length of the pore: $T = \mathbf{H}^2/D$. Thus, \hat{t} is re-scaled as

$$187 \quad \tilde{t} = \hat{t}/T.$$

Table 2: Table of Non-dimensional Parameters

Description	Symbol	Value
Aspect ratio	ϵ	$\frac{R}{H}$
Peclet number (evaporation rate)	β	$\frac{E_0 H}{D}$
Damkohler number (deposition rate)	ω	$\frac{\lambda H^2}{DR}$
Volume scaling fraction	γ	χC_{sat}
Initial concentration scaling	ρ	C_0/C_{sat}

188 These re-scales are then applied to concentration, radius, and precipitation flux function of
 189 the model, generating

$$190 \quad \widehat{C}(\hat{x}, \hat{z}, \hat{t}) = C_{sat} \tilde{C}(\tilde{x}, \tilde{z}, \tilde{t}), \quad \widehat{R}(\hat{z}, \hat{t}) = R \tilde{R}(\tilde{z}, \tilde{t}), \quad \widehat{Q}(\widehat{C}) = \lambda C_{sat} \tilde{Q}(\tilde{C}),$$

191 where now the precipitation flux is $\tilde{Q}(\tilde{C}) = \max(\tilde{C} - 1, 0)$. These scaled variables and functions
 192 replace the dimensional counterparts in the previous equations. The dimensionless height
 193 (2.11) is then

$$194 \quad (2.12) \quad \tilde{H}(\tilde{t}) = 1 - \beta \tilde{t},$$

195 where the Péclet number β is adopted to describe the evaporation rate. Furthermore, other
 196 dimensional constants are replaced with non-dimensional parameters, where a summary of
 197 all dimensionless parameters is listed in Table 2. For example, aspect ratio $\epsilon = R/H$ is
 198 used to define the geometry of the pore, and if the pore is long and narrow, ϵ approaches
 199 zero. That is, the original diffusion equation and boundary conditions are first scaled with
 200 the scaled coefficients, and then the non-dimensional parameters are substituted. The 2D
 201 diffusion equation (2.3) becomes

$$202 \quad (2.13) \quad \epsilon^2 \tilde{C}_{\tilde{t}} = \tilde{C}_{\tilde{x}\tilde{x}} + \epsilon^2 \tilde{C}_{\tilde{z}\tilde{z}}.$$

203 The boundary conditions at the bottom and left reflecting surfaces (2.4) remain

$$204 \quad (2.14) \quad \tilde{C}_{\tilde{z}} = 0 \quad \tilde{C}_{\tilde{x}} = 0.$$

205 The boundary condition for the top surface (2.6) transforms to

$$206 \quad (2.15) \quad \beta \tilde{C} - \tilde{C}_{\tilde{z}} = 0,$$

207 The right boundary condition with flux due to deposition (2.8) is calculated as

$$208 \quad (2.16) \quad \epsilon^2 (\tilde{C}_{\tilde{z}} \tilde{R}_{\tilde{z}} - \tilde{C} \tilde{R}_{\tilde{t}}) - \tilde{C}_{\tilde{x}} = \omega \epsilon^2 \tilde{Q}(\tilde{C}) \sqrt{1 + \epsilon^2 (\tilde{R}_{\tilde{z}})^2}$$

209 with ω acting as a deposition rate. The rescaled equation for the evolution of the wall (2.9)
 210 is now

$$211 \quad (2.17) \quad \epsilon^2 \tilde{R}_{\tilde{t}} = -\omega\gamma\epsilon^2 \tilde{Q}(\tilde{C}) \sqrt{1 + \epsilon^2 (\tilde{R}_{\tilde{z}})^2}$$

212 with γ incorporated as the non-dimensional volume scaling coefficient. The initial conditions
 213 for the non-dimensional model becomes

$$214 \quad (2.18) \quad \tilde{C}(\tilde{x}, \tilde{z}, 0) = \rho, \quad \tilde{R}(\tilde{z}, 0) = 1, \quad \tilde{H}(0) = 1.$$

215 In the next section, we execute a change of variables to simplify numerical computation. The
 216 motivation behind having this nondimensionalized and non-computationally modified version
 217 of the system as an intermediate step is to use it for asymptotically reducing the model which
 218 is described later in the paper.

219 **2.1.2. Computational Method.** To produce an accurate study of the particle concen-
 220 tration in the irregular domain due to the nonuniform pore wall, a numerical approach of
 221 transforming the physical domain onto a fixed computational domain is applied. This trans-
 222 formation is necessary because finite difference methods provide limited spatial resolution,
 223 which cannot fully capture the irregular shape of the boundary over time. Without compu-
 224 tational scaling, finite difference methods would introduce errors when calculating flux and
 225 when applying boundary conditions, often causing the system to lose mass. Therefore, the
 226 moving boundary problem is mapped onto fixed computational domains in both the \tilde{x} and \tilde{z}
 227 direction. This is done by scaling

$$228 \quad x = \frac{\tilde{x}}{\tilde{R}(\tilde{z}, \tilde{t})}, \quad z = \frac{\tilde{z}}{\tilde{H}(\tilde{t})}, \quad t = \tilde{t},$$

229 such that $x \in [0, 1]$ and $z \in [0, 1]$. To define $C(x, z, t)$ and $R(z, t)$, we apply the following
 230 change of variables,

$$231 \quad (2.19) \quad \tilde{C}(\tilde{x}, \tilde{z}, \tilde{t}) = C\left(\frac{\tilde{x}}{\tilde{R}(\tilde{z}, \tilde{t})}, \frac{\tilde{z}}{\tilde{H}(\tilde{t})}, \tilde{t}\right), \quad \tilde{R}(\tilde{z}, \tilde{t}) = R\left(\frac{\tilde{z}}{\tilde{H}(\tilde{t})}, \tilde{t}\right).$$

232 Substituting the scaled variables x and z and the scaled functions C and R into the system
 233 of non-dimensionalized PDEs describing the simplified 2D pore channel problem, Equation
 234 (2.13) simulating the main fluid body becomes

$$235 \quad (2.20) \quad \epsilon^2 \left(C_t + \frac{z\beta}{H} C_z + \left(\frac{x}{R} \frac{z\beta R_z}{H} - \frac{xR_t}{R} - \frac{2xR_z^2}{R^2 H^2} + \frac{xR_{zz}}{RH^2} \right) C_x \right) =$$

$$236 \quad \frac{1}{R^2} C_{xx} + \epsilon^2 \left(-\frac{2xR_z}{RH^2} C_{xz} + \left(\frac{xR_z}{RH} \right)^2 C_{xx} + \frac{1}{H^2} C_{zz} \right).$$

237 The new equation holds on the computational domain $[0, 1] \times [0, 1]$ and the four boundary
 238 conditions are then transformed into

$$239 \quad (2.21) \quad \left[\epsilon^2 \left\{ -C \left(R_t - \frac{zR_z}{H^2} \right) + \frac{R_z}{H} \left(\frac{C_z}{H} - \frac{C_x R_z}{R^2 H} \right) \right\} - \frac{C_x}{R} \right]_{x=1} = \omega\epsilon^2 Q(C) \sqrt{1 + \epsilon^2 \frac{1}{H^2} R_z^2},$$

$$240 \quad (2.22) \quad \left[-\frac{C_z}{H} \right]_{z=1} = 0, \quad \frac{1}{R} C_x \Big|_{x=0} = 0, \quad \frac{1}{H} C_z \Big|_{z=0} = 0,$$

241 and the deposition equation that describes the evolution of the wall geometry

$$242 \quad (2.23) \quad \epsilon^2 \left(R_t - \frac{\beta z}{H^2} R_z \right) = -\omega \gamma \epsilon^2 Q(C) \sqrt{1 + \frac{\epsilon^2 R_z^2}{H^2}}.$$

243 The system of non-dimensionalized PDEs on the computational domain is solved in MATLAB,
 244 making use of the forward Euler method in time with an upwind scheme for Equation (2.23)
 245 and a centered finite difference method in space for Equation (2.20). One-sided derivatives
 246 were used for boundary conditions. Table 1 summarizes parameters like evaporation rate,
 247 precipitation rate, and other initial conditions used in the model and gives example values
 248 used in determining a computational solution. We may also use a range of values for each
 249 parameter that we use to systematically analyze the model's behavior.

250 **3. SDE problem.** A stochastic representation for the particle concentration will allow for
 251 simulations of individual particle trajectories and a particle-level understanding of the model.
 252 In higher dimensions, SDEs can be less computationally demanding than finite difference
 253 methods for PDEs and can operate on parallel machines [9]. Diffusion of particle concentration
 254 is inherently stochastic and is described by Brownian motion [11]. Equation (2.3) models 2D
 255 isotropic diffusion and can be expressed in terms of the SDEs

$$256 \quad (3.1) \quad d\hat{X}_t = \hat{\sigma}_x dW_t \quad d\hat{Z}_t = \hat{\sigma}_z dW_t.$$

257 Here, a standard Wiener process (i.e. Brownian motion) is comprised of $dW_t \sim \mathcal{N}(0, \Delta t)$ and
 258 $\hat{\sigma}$ is found from the diffusion constant D with the relationship $\hat{\sigma}_x = \hat{\sigma}_z = \sqrt{2D}$. However,
 259 in the nondimensionalized diffusion equation, Equation (2.13), the diffusion coefficient is re-
 260 scaled in the \tilde{X} and \tilde{Z} directions, and is dependent on the parameter ϵ . Values for $\tilde{\sigma}_x$ and $\tilde{\sigma}_z$
 261 are $\sqrt{2}/\epsilon$ and $\sqrt{2}$, respectively.

262 In the computational version of the problem, additional drift terms μ are generated and
 263 diffusion σ in the x and z directions also become interdependent. Written in vector form, the
 264 resultant stochastic process becomes

$$265 \quad (3.2) \quad d\vec{X}_t = \vec{\mu}(\vec{X}_t, t)dt + \boldsymbol{\sigma}(\vec{X}_t, t)d\vec{W}_t,$$

266 where $\vec{\mu}$ is the drift vector, $\vec{X}_t = (X_t, Z_t)$, and $\boldsymbol{\sigma}$ is a 2 by 2 matrix found from the diffusion
 267 tensor $D = \frac{1}{2}\boldsymbol{\sigma}\boldsymbol{\sigma}^\top$. The density function for the distribution of \vec{X}_t is governed by the Fokker-
 268 Planck (FP) equation [11]. In 2D, the FP equation for $C(x, z, t)$ is

$$269 \quad (3.3) \quad \frac{\partial C}{\partial t} + \frac{\partial}{\partial x}(\mu_x C) + \frac{\partial}{\partial z}(\mu_z C) = \frac{\partial^2}{\partial x^2}(D_{xx}(x, z, t)C) +$$

$$270 \quad 2\frac{\partial^2}{\partial z \partial x}(D_{xz}(x, z, t)C) + \frac{\partial^2}{\partial z^2}(D_{zz}(x, z, t)C),$$

271 which comes in similar form as our 2D diffusion equation (2.20) in the computational domain:

$$272 \quad (3.4) \quad C_t + \left(\frac{x}{R} \frac{z\beta R_z}{H} - \frac{xR_t}{R} - \frac{2xR_z^2}{R^2 H^2} + \frac{xR_{zz}}{RH^2} \right) C_x + \frac{z\beta}{H} C_z =$$

$$273 \quad \left(\frac{1}{\epsilon^2 R^2} + \left(\frac{xR_z}{RH} \right)^2 \right) C_{xx} - \frac{2xR_z}{RH^2} C_{xz} + \frac{1}{H^2} C_{zz}.$$

274 We proceed with matching terms between Equations (3.3) and (3.4) (i.e. time derivatives
 275 term, diffusive terms with second partials, advective terms with first partials) to obtain forms
 276 for the drift and diffusion coefficients, $\mu(x, z, t)$ and $\sigma(x, z, t)$. Then, application of these
 277 coefficients to Equation (3.2) gives an SDE representation of the 2D scaled model.

278 Discretization of the SDE model relies on the Euler-Maruyama method, commonly used
 279 to simulate SDEs. The numerical approximation of Equation (3.2) becomes $\vec{X}_{t+\Delta t} - \vec{X}_t =$
 280 $\vec{\mu}(\vec{X}_t, t)\Delta t + \sigma\Delta\vec{W}_t$. If we let $\zeta_i := \frac{1}{\sqrt{\Delta t}}\Delta W_{i,t} \sim \mathcal{N}(0, 1)$, the step equations that govern all
 281 numerics for this SDE system are

$$282 \quad (3.5) \quad \begin{aligned} X_{t+\Delta t} - X_t &= \mu_x\Delta t + (\sigma_{xx}\zeta_X + \sigma_{xz}\zeta_Z)\sqrt{\Delta t} \\ 283 \quad Z_{t+\Delta t} - Z_t &= \mu_z\Delta t + (\sigma_{xz}\zeta_X + \sigma_{zz}\zeta_Z)\sqrt{\Delta t} \end{aligned}$$

284 with, again, ζ_X and ζ_Z composing a 2D standard Wiener process.

285 **3.1. Boundary Conditions and Deposition Algorithm.** The 2D SDE model consists of
 286 an ensemble of individual particle trajectories over time, where particles move freely in the
 287 fluid until encountering a boundary. The stochastic models in the previous section do not
 288 incorporate the influence of any boundary conditions. To supplement the SDE with boundary
 289 conditions, we have reflective boundary conditions following Erban and Chapman’s algorithm
 290 for simple reflective boundary conditions [3]. Rather than the approach for Robin boundary
 291 condition proved in Leimkuhler et al. [9], we instead describe the moving boundary condition
 292 with flux by probability function (3.6). Particles that hit the wall, $X_t = 1$, may be deposited
 293 depending on the local concentration of particles. The concentration will be calculated as the
 294 number particles in a small area near the wall divided by that area. If concentration near the
 295 wall is above the threshold $C = 1$, our approximation is to take the probability that particles
 296 hitting the wall actually deposit as

$$297 \quad (3.6) \quad P(C) = \begin{cases} 1 - e^{-k(C-1)} & C \geq 1, \\ 0 & C < 1. \end{cases}$$

298 This probability increases to 1 as C becomes large, and also includes the small possibility that
 299 particles do not deposit despite the concentration being over-saturated. After finding $P(C)$,
 300 we generate a uniform random number and determine whether it is above $P(C)$, depositing
 301 the particle if so. This is an empirical approach for describing deposition at the wall and is not
 302 guaranteed to match with boundary condition (2.21), but it was observed to give reasonable
 303 agreement.

304 A representative step $(X_t, Z_t) \rightarrow (X_{t+\Delta t}, Z_{t+\Delta t})$ with conditions at all four boundaries
 305 is described by the algorithm in Algorithm 3.1 [3]. All coordinates are scaled to a fixed
 306 computational domain similar to the PDE model, so particles must stay in the domain $[0, 1] \times$
 307 $[0, 1]$. In the algorithm, a uniform random variable, called U with $0 \leq U \leq 1$, is compared
 308 against $P(C)$. If $U < P(C)$, the particle trajectory is terminated due to deposition. If
 309 deposition occurs, the wall inches into the fluid and the radius decreases by a small amount δ ,
 310 set to be around 0.1-1% the width of the pore [12]. Similar to how the volume scaling fraction
 311 γ in the PDE model accounts for reduction in particle size after deposition, δ is set to be a

Algorithm 3.1 Particle Trajectory $(X_t, Z_t) \rightarrow (X_{t+\Delta t}, Z_{t+\Delta t})$

Given X_t , Z_t , t , and $C(X_t, Z_t, t)$, compute $(X_{t+\Delta t}, Z_{t+\Delta t})$ from Equation (3.5). Also, calculate probability $P(C_t)$ based on an average C_t according to the number of particles in a small neighborhood of the wall at height Z_t .

```

while  $Z_{t+\Delta t} < 0$  or  $Z_{t+\Delta t} > 1$  do
  if  $Z_{t+\Delta t} < 0$  then
    Reflect:  $Z_{t+\Delta t} = -Z_{t+\Delta t}$ 
  end if
  if  $Z_{t+\Delta t} > 1$  then
    Reflect:  $Z_{t+\Delta t} = 2 - Z_{t+\Delta t}$ 
  end if
end while
while  $X_{t+\Delta t} < 0$  or  $X_{t+\Delta t} > 1$  do
  if  $X_{t+\Delta t} < 0$  then
    Reflect:  $X_{t+\Delta t} = -X_{t+\Delta t}$ 
  end if
  if  $X_{t+\Delta t} > 1$  then
    Calculate probability  $P(C_t)$  from Equation (3.6) and generate a uniform random number  $U$  from (0,1)
    if  $U < P(C_t)$  then
      Terminate particle trajectory and decrease pore radius by approximated particle size at height  $Z_t$  (deposition)
    else
      Reflect:  $X_{t+\Delta t} = 2 - X_{t+\Delta t}$ 
    end if
  end if
end while
return  $(X_{t+\Delta t}, Z_{t+\Delta t})$ 

```

312 small particle size relative to the pore channel. As evaporation occurs, particles in the main
313 fluid body are computationally scaled, but the pore channel radius is not. Thus, in response to
314 the fluid level lowering, the number of particles deposited on the walls is distributed according
315 to a new partition of the radius in order to preserve mass. In Equation (3.6), the parameter
316 k is a constant chosen to minimize mean-squared error (MSE) between the dry deposition
317 patterns of the PDE and SDE model. To determine this constant, we found values for k
318 across different initial conditions where the MSE is minimized, then the average, $k = 0.036$,
319 is taken as the constant. As MSE is calculated with simulations of PDE model with fixed
320 parameters, k has a correspondence with the parameter λ in the PDE model, or ω after non-
321 dimensionalization (See Table 1). And so, fitting $k = 0.036$ only applies for the particular
322 values of λ used in the minimization of the MSE, but a relationship between k and λ can be
323 determined. While Leimkuhler et al. proposed a sophisticated stochastic approximation for
324 Robin boundary conditions, comparisons of (3.6) with the PDE model given in Section 5 show

325 this to be a simpler, yet physically reasonable formulation for deposition. We recognize that
 326 the choice for (3.6) breaks the mathematical connection between the PDE and SDE boundary
 327 conditions, but also highlight that even with its simplicity it can capture the physical process
 328 of deposition and produce comparable deposition results.

329 **4. 1D Asymptotic problem.** Using the same nondimensionalized parameters from Ta-
 330 ble 2, we now let $\epsilon \rightarrow 0$, which implies \mathbf{R}/\mathbf{H} will approach zero. Recalling that ω , appearing
 331 in equations (2.8) and (2.9), is defined as $\frac{\lambda \mathbf{H}^2}{D \mathbf{R}}$, if the other dimensional values are held con-
 332 stant, ω will approach infinity. But introducing a new parameter ψ such that the relation
 333 $\lambda = \psi \epsilon$ holds with ψ held constant will prevent ω from producing singular limits. In Equation
 334 (2.13), by letting ϵ go to zero, perturbation expansions for both \tilde{C} and \tilde{R} to their second lead-
 335 ing order terms with respect to ϵ^2 are $\tilde{C} = \tilde{C}_0 + \epsilon^2 \tilde{C}_2 + O(\epsilon^4)$, $\tilde{R} = \tilde{R}_0 + \epsilon^2 \tilde{R}_2 + O(\epsilon^4)[1]$. We
 336 group by powers of ϵ for the diffusion equation (Equation (2.13)) and each boundary condition
 337 (Equations (2.14)-(2.17)) at $O(\epsilon^0)$ and $O(\epsilon^2)$. Grouped by order, the $O(\epsilon^0)$ sub-problem can
 338 be written as

$$\tilde{C}_{0\tilde{x}\tilde{x}} = 0, \quad \beta \tilde{C}_0 - \tilde{C}_{0\tilde{z}} = 0 \Big|_{\tilde{z}=\tilde{H}}, \quad \tilde{C}_{0\tilde{z}} = 0 \Big|_{\tilde{z}=0}, \quad \tilde{C}_{0\tilde{x}} = 0 \Big|_{\tilde{x}=0, \tilde{R}_0}$$

In $O(\epsilon^0)$, $\tilde{C}_{0\tilde{x}\tilde{x}} = 0$ is the PDE representing the system, and $\beta \tilde{C}_0 - \tilde{C}_{0\tilde{z}} = 0$ represents the
 top boundary, $\tilde{C}_{0\tilde{z}} = 0$ represents the bottom boundary, and $\tilde{C}_{0\tilde{x}} = 0|_{\tilde{x}=0, \tilde{R}_0}$ represents the
 left and right boundaries. The $O(\epsilon^2)$ sub-problem is

$$\begin{aligned} \tilde{C}_{2\tilde{x}\tilde{x}} + \tilde{C}_{0\tilde{z}\tilde{z}} - \tilde{C}_{0\tilde{t}} = 0, \quad \beta \tilde{C}_2 - \tilde{C}_{2\tilde{z}} = 0, \quad -\tilde{C}_{2\tilde{x}} - \tilde{Q}(\tilde{C}_0)\omega - \tilde{C}_0 \tilde{R}_{0\tilde{t}} + \tilde{C}_{0\tilde{z}} \tilde{R}_{0\tilde{z}} = 0, \\ \tilde{Q}(\tilde{C}_0)\omega\gamma + \tilde{R}_{0\tilde{t}} = 0. \end{aligned}$$

339 Solving for \tilde{C}_0 by integration and using boundary conditions at the top and bottom reveal
 340 that \tilde{C}_0 is independent of \tilde{x} . Further substitution derives the following asymptotically reduced
 341 equation for the model:

$$342 \quad (4.1a) \quad -\tilde{Q}(\tilde{C}_0)\omega + \tilde{R}_0(\tilde{C}_{0\tilde{t}} - \tilde{C}_{0\tilde{z}\tilde{z}}) - \tilde{C}_0 \tilde{R}_{0\tilde{z}} + \tilde{C}_{0\tilde{z}} \tilde{R}_{0\tilde{z}} = 0$$

343

$$344 \quad (4.1b) \quad \tilde{R}_{0\tilde{t}} = -\tilde{Q}(\tilde{C}_0)\omega\gamma$$

345 The simplified equation with its boundary conditions is

$$346 \quad (4.2a) \quad (\tilde{C}\tilde{R})_{\tilde{t}} = (\tilde{C}_{\tilde{z}}\tilde{R})_{\tilde{z}} - \omega\tilde{Q}(\tilde{C}), \quad 0 \leq \tilde{z} \leq 1 - \beta\tilde{t}$$

347

$$348 \quad (4.2b) \quad \left(\beta \tilde{C} - \tilde{C}_{\tilde{z}} \right) \Big|_{\tilde{z}=1-\beta\tilde{t}} = 0, \quad \tilde{C}_{\tilde{z}} \Big|_{\tilde{z}=0} = 0$$

349 with initial conditions $\tilde{H}(0) = 1, \tilde{R}(\tilde{z}, 0) = 1, \tilde{C}(\tilde{z}, 0) = \rho$. With the asymptotic model, a
 350 change in variables was performed similar to that of the computational version of the main
 351 PDE as seen in Section 2.1.2.

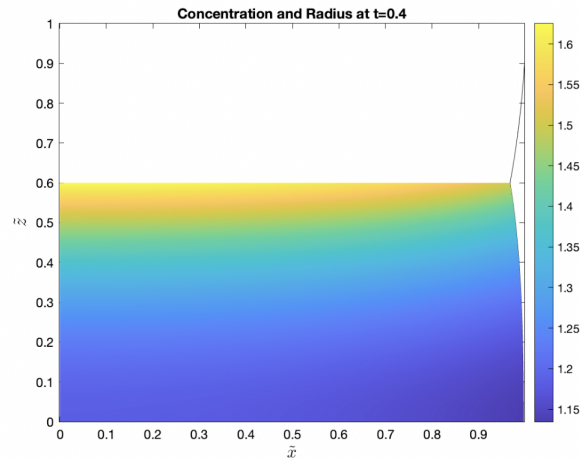


Figure 2: Concentration color plot and deposition pattern of the 2D PDE model at $t = 0.4$ with $\beta = 1$, $\omega = 0.6$, and $\mathbf{R} = 1$.

352 **5. Comparison of Results in Pore Channel Geometry.** In this section, results from the
 353 1D asymptotic model and the SDE model are compared against the 2D PDE problem. Pore
 354 evolution, concentration evolution, and deposition mass are analyzed as a means of determin-
 355 ing if models corroborate each other.

356 **5.1. 2D PDE vs. 1D Asymptotic PDE.** When the evaporating interface reaches a small
 357 height, the diminishing fluid volume and the increasing concentration of particles causes the
 358 model to enter a high concentration regime. Given that the model is dependent upon the
 359 assumption that particles have negligible volume, we no longer have confidence in the model
 360 when the concentration is no longer dilute. For all following results, simulations terminate at
 361 around heights 0.2 or 0.3, chosen from observation based on the combination of parameters
 362 in Table 1 as an estimation of the margin before the remaining fluid becomes too dense.

363 Figure 2 is a color plot of particle concentration when fluid height reaches 0.6 with $\beta = 1$.
 364 The figure is not displayed in the computational domain but in the non-dimensionalized
 365 physical \tilde{x} - \tilde{z} plane. The radius profile is $\tilde{R}_{full}(\tilde{z}, \tilde{t})$, but plotted with inverted axes to visually
 366 show how a deposition pattern may appear on a vertical pore channel wall. Greater adsorption
 367 occurs where local concentration far exceeds saturation ($\tilde{C} > 1$), which we can see is most
 368 common near the evaporating surface, where the yellow color demonstrates highest particle
 369 concentration. Concentration is usually highest at the surface due to evaporation, and thus,
 370 regardless of different initial conditions, the pore radius at the surface will also be the narrowest
 371 at the current fluid height. Note that concentration is relatively uniform across \tilde{x} , besides
 372 slightly higher values towards the top center of the pore. Thus, averaging concentration
 373 values across \tilde{x} will give a representative measurement of particle concentration at a given
 374 height \tilde{x} . In order to reduce the multi-variate function \tilde{C} shown in the color plot to 1D

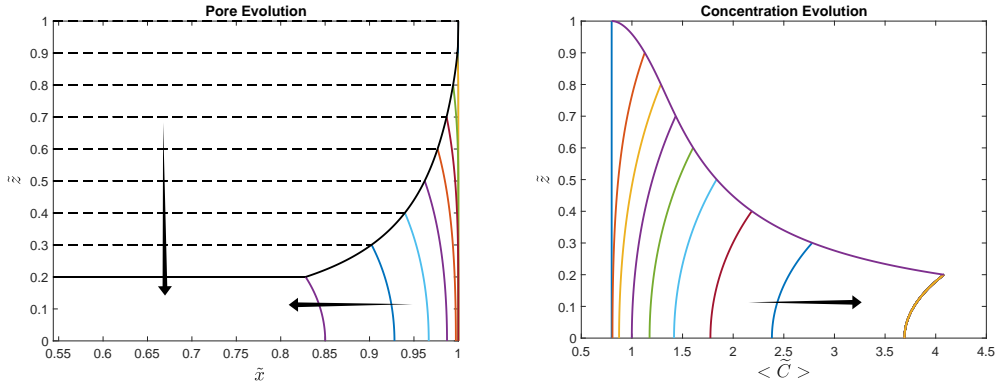


Figure 3: Evolution profiles produced by the 2D PDE model with $\mathbf{R} = 1$ and $\rho = 0.8$. Left: Pore Wall Evolution. Dotted lines demonstrate the decreasing fluid surface level at specific times, and arrows indicate the direction of motion for top and right boundaries. The figure shows individual pore radius profiles found at separate times that illustrate how the interface between accumulated particles and the fluid moves into the fluid over time. A solid curve connecting these profiles shows an interface between accumulated particles and the air as the fluid level lowers. Right: Concentration Evolution. The arrow shows direction of concentration evolution over time. Similarly, individual curves are separate concentration profiles at different times, determined from taking the mean concentration across \tilde{x} for a given \tilde{z} . All profiles are connected by a solid line that demonstrates concentration increasing monotonically.

375 curves, we find

376 (5.1)
$$\langle \tilde{C} \rangle := \frac{1}{\tilde{R}} \int_0^{\tilde{R}} \tilde{C}(\tilde{x}, \tilde{z}, \tilde{t}) d\tilde{x}.$$

377 **Figure 3** is an example of a pore radius evolution plot and its corresponding concentration
 378 evolution plot. In **Figure 3** (left), the horizontal arrow indicates the pore radius narrowing
 379 inward over time due to deposition and the vertical arrow illustrates the fluid height decreasing
 380 during evaporation. Curves drawn at each 0.1 decrease in fluid height show particle deposition
 381 adding mass to the changing pore wall. $\tilde{R}_{dry}(\tilde{z})$ lies above the fluid-air interface. At $\tilde{t} = 0.8$,
 382 the dry region above $\tilde{z} = 0.2$ (solid black line) is fixed and no longer experiences deposition,
 383 while anything below the black line is still submerged in fluid. We also plot the lowering
 384 interface with dashed black lines at each 0.1 increment. It is also noticeable in the figure that
 385 deposition does not begin immediately. Instead, deposition starts at around $\tilde{z} = 0.95$ due to
 386 the fluid starting under-saturated at $\rho = 0.8$.

387 The concentration evolution graph uses Equation (5.1) to find 1D concentration profiles,
 388 and plots them sideways to match the pore radius evolution graph. The initial profile in
 389 **Figure 3** (right) is vertical line at ρ , with uniform concentration and no change in the system
 390 yet. Again at every 0.1 decrease in height, we plot the 1D curve at each time step, signified
 391 by different colors. The concentration is not uniform at each $\tilde{z} \neq 0$. The arrow further

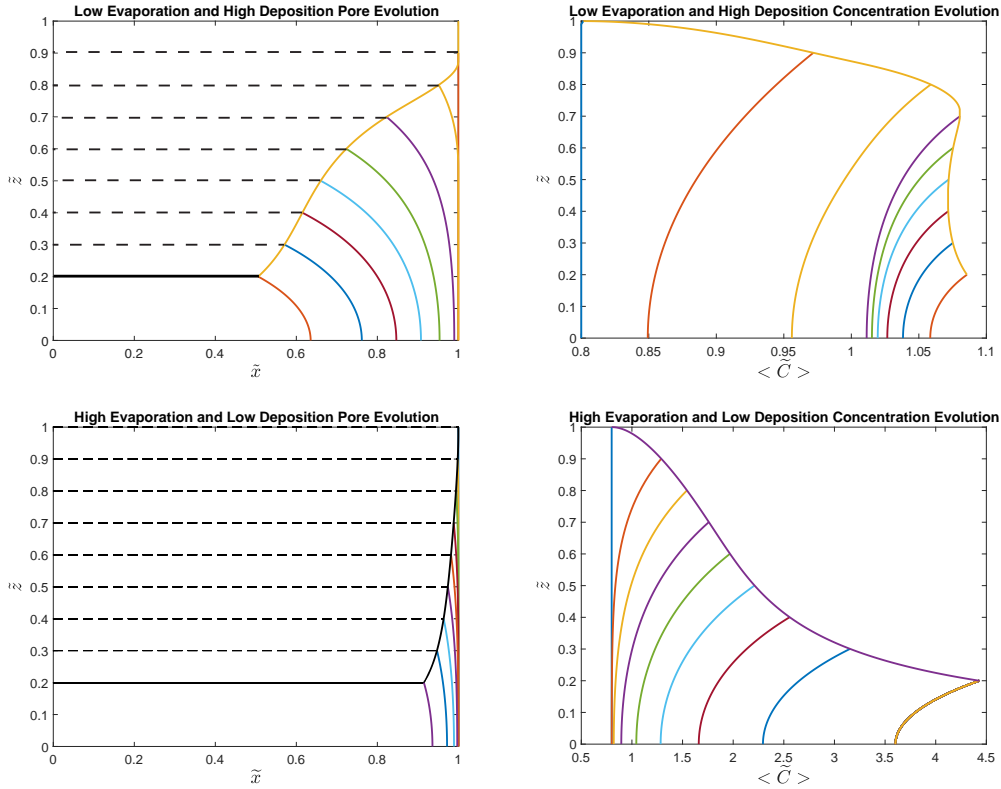


Figure 4: Pore radius and concentration evolution graphs for different combinations of evaporation (β) and deposition (ω) rates. Top row: low $\beta = 0.3$, high $\omega = 8$, $\rho = 0.8$, and $\gamma = 0.4$. Bottom row: high $\beta = 2$, low $\omega = 1$, $\rho = 0.8$, and $\gamma = 0.4$.

392 demonstrates to read the plot from left to right, since generally, the concentration increases
 393 as the height of the pore decreases. In both plots, we end the simulation at $\tilde{z} = 0.2$.

394 Deposition coefficient ω and evaporation rate β can be altered to investigate variations in
 395 the radius and concentration evolution. The radius evolution graph in Figure 4 reveals that
 396 a higher deposition rate coupled with a lower evaporation rate results in the radius rapidly
 397 shooting inward after a delayed initiation of deposition at around $\tilde{z} = 0.85$. For concentration,
 398 on the other hand, the low β high ω parameter combination leads to a drastic increase in fluid
 399 concentration towards the beginning but slows down dramatically after the fluid height reaches
 400 0.7. Where there are high evaporation and low deposition rates instead, we see significantly
 401 less deposition and a concentration profile with larger concentration values in general. Faster
 402 evaporation limits the time for particles to accumulate, while a lower deposition rate prevents
 403 deposition despite a high local concentration.

404 Figure 5 displays changes in $\tilde{R}(\tilde{z}, \tilde{t})$ due to various values for \mathbf{R} , the initial pore width, in
 405 both the PDE 2D model and the asymptotically reduced model. The left graph displays the
 406 decrease of radius due to deposition from initial radius, that is $\tilde{R}(\tilde{z}, 0.3) - \mathbf{R}$, with respect

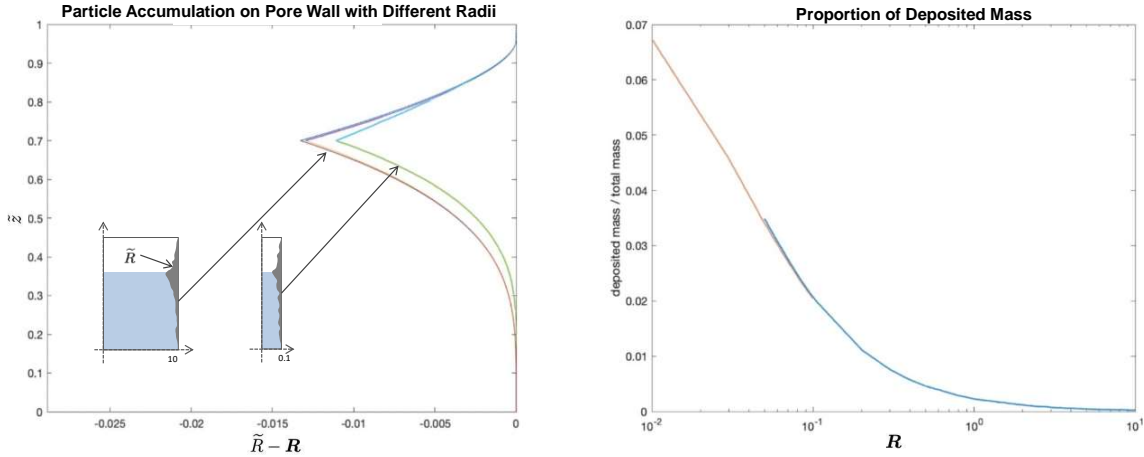


Figure 5: Left: The decrease of pore radius $\tilde{R}(\tilde{z}, 0.3) - R$

with different initial radius $R = 10$, $R = 1$, $R = 0.1$ from left to right when $\tilde{t} = 0.3$. Right: Mass of deposited particles/total particles with respect to initial radius R , with R on a logarithmic scale ($R = 0.01$ to $R = 0.1$ for asymptotic model (red); $R = 0.05$ to $R = 10$ for PDE 2D model (blue)).

407 to \tilde{z} at different initial radii. At $\epsilon = 0.1$, we only see one profile because the two models
 408 virtually overlap. The figure supports that as ϵ goes to zero, the results from the scaled
 409 2D PDE model approach those of the asymptotic PDE model. An examination of deposited
 410 mass further validates this notion. The right graph in Figure 5 shows deposited mass, scaled
 411 by initial mass, in both the PDE asymptotic model (red) and the primary PDE 2D model
 412 (blue). In the range $R \in [0.05, 0.1]$, there is a region where the two graphs coincide. Looking
 413 back at Figure 2, the general uniformity in concentration across \tilde{x} also suggests that the
 414 1D asymptotically reduced model is a good approximation of the 2D model. In fact, the
 415 simulation for Figure 2 was not performed with a small aspect ratio, where $\epsilon = 1$. Then,
 416 Figure 2 and Figure 5 both reveal that the asymptotic model is a reasonable approximation
 417 of the 2D model, especially at relatively small aspect ratios.

418 **5.2. Comparing PDE Model and SDE Model.** Pore evolution in the SDE 2D model can
 419 also be graphed with both dry and wet sections shown together at different times, shown in
 420 Figure 6. As described in Section 3.1, we calculate the probability that particles exit the
 421 fluid by measuring local concentration at the wall. As fluid evaporates, particles become more
 422 packed and dense, resulting in higher probability for deposition and thus a gradual decrease in
 423 pore radius over time. The SDE model was also simulated in MATLAB. Comparing the SDE
 424 and PDE models on the same graph in Figure 6 shows that the dry portions of the deposited
 425 pattern agree, even more so at earlier times. Deposition patterns in the wet sections are
 426 dissimilar; however, we observe that when more fluid evaporates, the accumulated dry patterns
 427 still match up well. Differences in the PDE and SDE models appear to emerge towards the

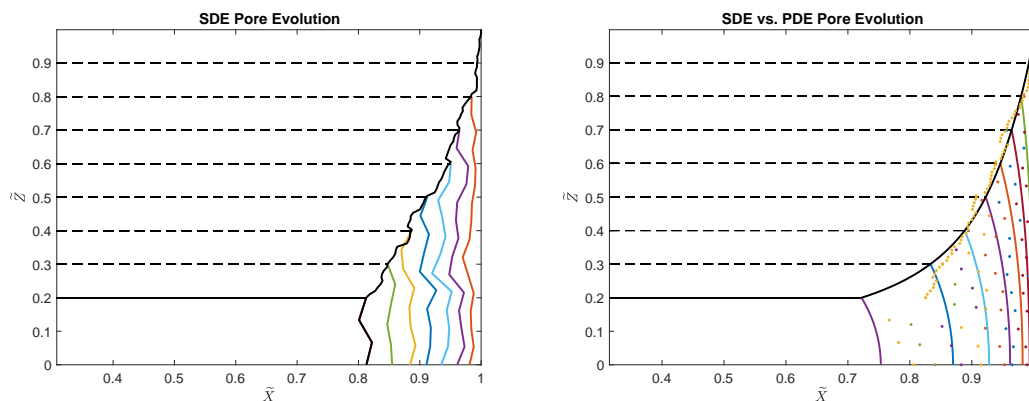


Figure 6: Left: Pore radius evolution of SDE model up until $t = 0.8$ and with $\rho = 1$, $D = 1$, and $E = 1$. Like previous figures, each colored, solid curve is a separate pore radius profile found at separate time points, with a black, solid line demonstrating the narrowing of the pore as time passes.

Right: Pore radius evolution of SDE (dotted) compared with the PDE (solid) 2D model at $t = 0.8$ with $\rho = 1$ or $C_0 = 0.5$, $D = 1$, and $\beta = 1$. The horizontal lines show the decreasing surface level of the evaporating fluid column.

428 end of the simulation, but at that time, both models may be inaccurate from failure in holding
 429 the dilute assumption.

430 In both models, accumulation on the walls shows a concave-up pattern, with the peak
 431 height of accumulation at the fluid-air interface. Figure 7 (left) is a graph of the maximum
 432 accumulation ($1 - \tilde{R}$) over time for one set of parameters, giving a percent error of 16.7% with
 433 the PDE model as the theoretical result. The right graph shows total dry mass over time,
 434 or total accumulation in $\tilde{R}_{dry}(\tilde{z})$. There is close agreement between the two models, with a
 435 percent error of 5.4%.

436 We have observed general similarities between the SDE and PDE results, but we believe
 437 that differences appear from how boundary conditions are treated, particularly in the presence
 438 of flux or partial adsorption. Leimkuhler et al. [9] derived accurate stochastic Robin boundary
 439 conditions to approximate reflected stochastic differential equations, but to our knowledge,
 440 how to properly treat boundary conditions with flux, like Equation (2.21), has not been
 441 resolved. Our proposed probabilistic boundary condition in Algorithm 3.1 can at least produce
 442 comparable results for the dry portion of the deposition pattern in the dilute case.

443 **6. Parameter Analysis in the 2D Model.** This section explores how some of the param-
 444 eters listed in Table 2 influence model attributes, such as the pore radius at a given height
 445 or the monotonicity of the concentration evolution. Deposition and evaporation are noted as
 446 opposite processes, where the former decreases particle concentration within the fluid and the
 447 latter increases it. The combined mechanism is analyzed at different degrees by varying their
 448 rates.

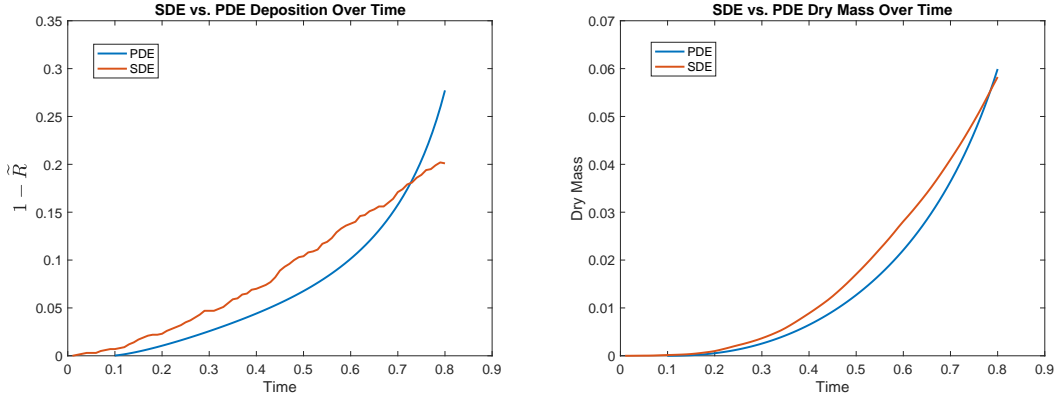


Figure 7: Left: Comparison of SDE and PDE maximum accumulation over time. \tilde{R} represents the minimal radius found in the pore radius profile, so with the pore radius non-dimensionalized to 1, $1 - \tilde{R}$ represents the maximum accumulation along the wall at each time.

Right: Comparison of SDE and PDE dry mass over time. Dry mass is calculated as the total accumulation at each time, integrating over the particle deposition pattern above the fluid-air interface. Both plots have simulations running until $t = 0.8$, with $D = 1$, $\rho = 1$ or $C_0 = 0.5$, and $\beta = 1$.

449 **6.1. Effects of Parameters.** Highlighting specific characteristics of the model by per-
 450 forming sensitivity analyses on model parameters can provide critical information to improve
 451 industrial design. For example, the distinction between brine water and pure water (differ-
 452 ences in concentration, evaporation rate, and concentration evolution) is crucial for designing
 453 anti-fouling/anti-salt accumulation solar evaporator technology for desalination [15].

454 For the following results, the system consistently evaporates to half height, or to 0.5 (with
 455 initial height of 1). First, we observe the relationship between pore radius at half height and
 456 parameters of interest. As expected, the radius decreases as the rate of deposition increases,
 457 though the negative relationship is not dramatic. We expect deposition and evaporation to
 458 work as opposing processes, where the former decreases particle concentration in the fluid
 459 and the latter increases concentration. Even when particles deposit from the fluid quickly,
 460 the rapid rate at which concentration is expected to change may be mitigated by a lower
 461 evaporation rate. Furthermore, the resulting radius at half height and evaporation rate have
 462 a positive relationship. Again, the rate at which the concentration changes is mitigated due
 463 to a higher evaporation rate and a relatively lower deposition rate, leading to a positive slope
 464 with small magnitude. In both cases, the concentration would fluctuate between being under
 465 and above saturation levels.

466 Other observations show that decreasing the initial concentration, ρ , results in pore radii
 467 that are significantly larger. The converse is also true: when ρ is higher, particle deposition
 468 is expected to occur earlier because ρ is initially closer to the saturation concentration. Ad-

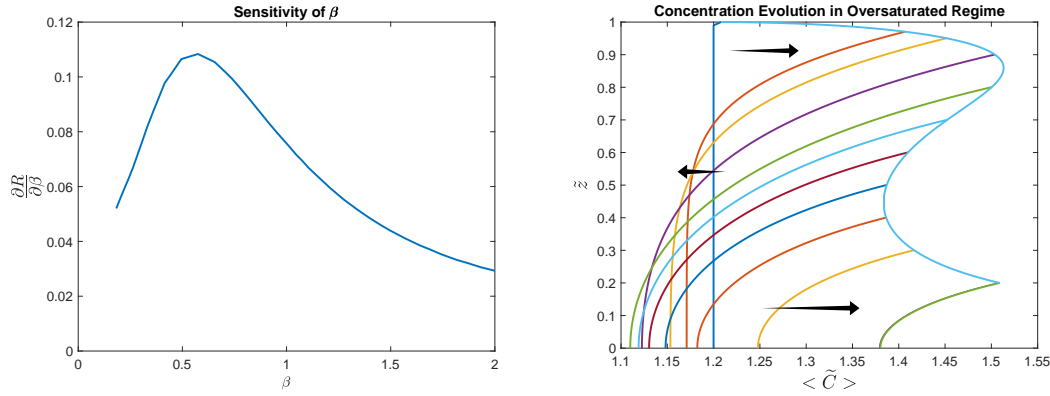


Figure 8: Left: $\partial R/\partial\beta$ (change in radius with respect to evaporation rate) at height 0.5 against varying values of β demonstrating a point of stability where the curve peaks. Right: Non-monotone concentration evolution with overlapping concentration curves in the oversaturated regime. Black arrows indicate that concentration at the fluid-air interface increases up to around height 0.85, decreases up to around height 0.45, and proceeds to increase again. This pattern is also shown by the curve connecting maximal concentration values for each concentration profile as the fluid-air interface lowers.

Simulations were performed with parameters $\beta = 1$, $\gamma = 0.4$, $\omega = 10$, and $\rho = 1.2$.

ditionally, an inverse relationship is observed between the pore radius and the volume scaling coefficient, γ . If γ is low, then there is less accumulation of particles inside of the pore. A higher value for γ implies that the pore would clog earlier. Thus, with increasing γ , the radius decreases continuously until it hits 0, since a radius cannot be negative.

In our investigation of these parameter properties, we are most interested how the system behaves when the evaporation rate β changes. It is not immediately obvious when exactly concentration reaches its saturation point. Figure 8 (left) displays results from a sensitivity analysis test of β and shows a curve is almost parabolic in a certain region. Therefore, there exists a point of stability at the critical point, where changes in β cause minimal changes in $\frac{dR}{d\beta}$. Labeling these points β^* , we seek to understand how stability changes when system parameters are altered. Relationships between β^* and both γ (volume scaling fraction) and ω (deposition rate) are found to be positive and monotonically increasing. This is because the system constantly seeks stability, correspondingly shifting the point of stability after changing some parameter. In other words, one can infer the influence of a balancing force; modifying γ and ω require corresponding changes in the point of stability.

6.2. Analyzing Monotonicity of Concentration. Again, due to assumptions, the radius must be monotonically decreasing; however, this is not the case for concentration. For example, Figure 8 (right) shows that in the heavily over-saturated regime, the concentration evolution is not monotonically increasing. This can be shown by the concentration increasing, then decreasing, and then increasing for parts of the profiles. Furthermore, this can be more

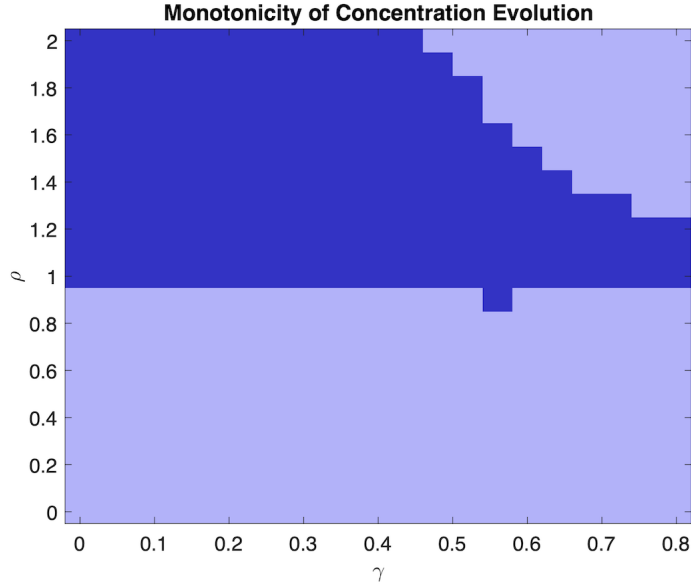


Figure 9: Regions of monotone vs. non-monotone concentration evolution according to variations in γ and ρ . Dark blue: non-monotone concentration evolution. Light blue: monotone concentration evolution.

489 easily identified by the fact that the concentration curves overlap, signifying a lack of mono-
 490 tonicity. To determine the criteria condition for non-monotone concentration evolution, the
 491 relationship between monotonicity of concentration evolution, ρ (scaled initial concentration),
 492 and γ is investigated. The result is demonstrated in the heat map [Figure 9](#), where dark blue
 493 represents non-monotone concentration evolution and light blue represents monotone concen-
 494 tration evolution, γ is the horizontal axis and ρ is the vertical axis. Concentration appears to
 495 be non-monotone for large ρ . However, some points beyond C_{sat} (i.e. $\rho = 2$) contain initial
 496 conditions that still produce a monotone concentration evolution, possibly due to model as-
 497 sumptions creating close relations between local concentration and concentration in the rest
 498 of the fluid. Model assumptions also neglect that drift velocity (assumed to be zero) within
 499 the fluid which can contribute to imbalances in concentration in the fluid.

500 **7. Droplet Model.** Previously, we discussed models in which it was assumed that fluids
 501 reached from end of the wall to the other. However, in events in which this may not occur,
 502 droplets may potentially form. With this in mind, the two most prevalent scenarios for
 503 modeling a droplet is fixing either the radius of the droplet or the contact angle [17]. This
 504 paper will work with the former, and models the droplet surface with the parabolic equation

505 (7.1)
$$\tilde{H}(\tilde{x}, \tilde{t}) = \tilde{h}(\tilde{t}) \left(1 - \left(\frac{\tilde{x}}{\mathbf{R}} \right)^2 \right),$$

506 where $\tilde{h}(\tilde{t}) = 1 - \beta\tilde{t}$ is the maximum height and \mathbf{R} is the fixed contact radius, set to 1. Again,
 507 only a half section of the 2D droplet is considered, drawn as a 2D parabola with an axis of
 508 symmetry at $\tilde{x} = 0$. In the PDE droplet model, the 2D nondimensionalized diffusion equation
 509 (2.13) is used to describe concentration within the droplet.

510 Discretizing the evolution of curved boundaries is more complex, so the top boundary
 511 of the droplet is approximated in a way that conserves particle mass. After evaporation,
 512 particles above the fluid-air interface are redistributed normal to the boundary, back into the
 513 computational domain. A fully absorbing boundary condition is chosen for the floor. Again,
 514 one-sided derivatives are implemented for the PDE boundary conditions.

515 The SDE algorithm is similar to the 2D model, where particles are reflected from the
 516 left and bottoms walls according to Algorithm 3.1; but, particles are reflected according to
 517 the normal vector at the boundary. Computational scaling for the droplet model in the SDE
 518 version of the droplet model similarly consists of bridging the scaled diffusion equation with
 519 the 2D FP equation, given by

$$\begin{aligned}
 & (7.2) \quad \frac{\partial C}{\partial t} - \frac{\partial C}{\partial z} \frac{\partial H}{\partial t} \frac{z}{H} = \\
 & D \left(\frac{\partial^2 C}{\partial x^2} - \frac{\partial^2 C}{\partial x \partial z} \frac{\partial H}{\partial x} \frac{z}{H} + \left(\frac{\partial H}{\partial t} \right)^2 \frac{\partial^2 C}{\partial z^2} \left(\frac{z}{H} \right)^2 + 2 \frac{\partial C}{\partial z} \left(\frac{\partial H}{\partial x} \right)^2 \frac{z}{H^2} - \frac{\partial C}{\partial z} \frac{\partial^2 H}{\partial x^2} \frac{z}{H} + \frac{\partial^2 C}{\partial z^2} \frac{1}{H^2} \right)
 \end{aligned}$$

522 for $0 \leq z \leq 1$. Matching the velocity terms and the scaled diffusion coefficients, again the 2
 523 by 2 matrix $\boldsymbol{\sigma}(\vec{x}, t)$ and the 2D vector $\vec{\mu}$ are solved for to write step equations just like (3.5).

524 **7.1. Droplet Results.** As previously mentioned, the PDE droplet has boundary condi-
 525 tions that match those of the SDE droplet in 1D. For the left boundary, one-sided Neumann
 526 boundaries are used in the PDE model and particles are reflected in the SDE model. At the
 527 floor, we implement a fully absorbing Dirichlet boundary for the PDE model and eliminate
 528 any trajectories that cross the floor for the SDE model. Unlike the 2D model, the droplet
 529 contains a non-flat surface, thus each surface grid point is given an averaged corner boundary,
 530 with one-sided derivatives following the equation $DC_x + \frac{\partial H(x,t)}{\partial t} C = 0$. We compare the SDE
 531 and PDE model with a fully absorbing floor in Figure 10. The highest concentration of par-
 532 ticles occurs at the top center of the droplet and disperses as they reach the floor, where they
 533 are 100% absorbed. However, due to the curved surface, the gradient is not uniform across
 534 the horizontal, leaving the corner with the least amount of particles. This pattern can be seen
 535 in both cases.

536 The sparsity of particles at the corner of the droplet may be attributed to 1) a lower number
 537 of particles reaching the corner or 2) more immediate absorption due to closer proximity to
 538 the floor. To determine which reason is more dominant, flux out of bottom of the droplet is
 539 observed for the PDE and SDE cases. For the PDE, flux is calculated at $z = 0$ using $-D \frac{\partial C}{\partial z}$,
 540 whereas its SDE counterpart simply counts the number of particle trajectories eliminated from
 541 the fluid after touching the floor. In Figure 11, both measurements of flux display similarly-
 542 shaped monotone decreasing curves, describing higher flux near the center of the droplet and
 543 less at the corner. If the sparsity of particles were attributed to faster adsorption (from a lower
 544 droplet height), the curves would be monotone increasing. Low flux at the corner indicates a

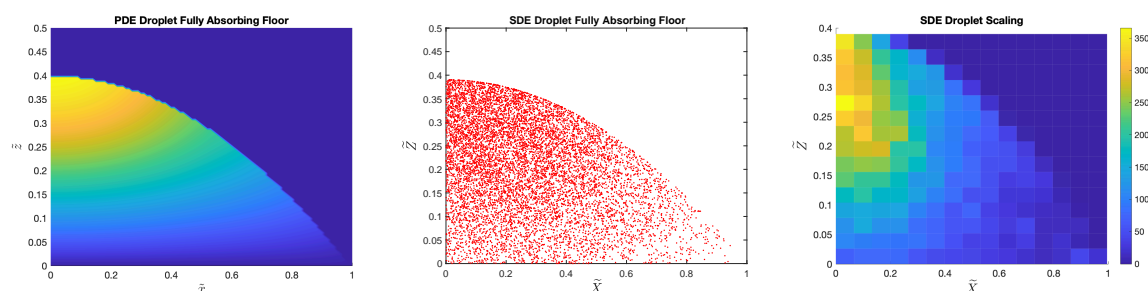


Figure 10: Particle distribution within a droplet with a fully absorbing floor. Parameters are $H_0 = 0.5, H_{end} = 0.4, D = 1, N = 40000$. Left: PDE with approximated boundary conditions. Middle: SDE with approximated boundary conditions. Right: SDE on a fixed computational domain with a partially absorbing floor.

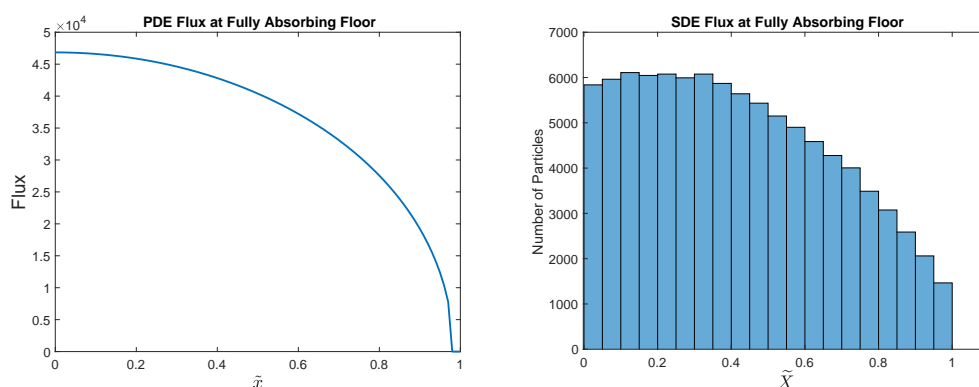


Figure 11: Flux distribution of a droplet with $H_0 = 0.5, H_{end} = 0.3, D = 1, n = 40000$ particles. Left: PDE, Right: SDE.

545 lower number of particles reaching the droplet corner. For that reason, we expect no coffee
 546 ring effect [5]. This corroborates with assumptions because the model neglects surface tension
 547 properties needed to precipitate a ring of particles at the edge of the droplet.

548 The rightmost graph in Figure 10 is a heat map of particle concentration in a compu-
 549 tationally scaled version of the SDE modeled droplet. Again, the Euler-Maruyama Method
 550 was used to approximate the SDEs found from Equation (7.2) for particles within the fluid
 551 body. A partially absorbing boundary is set at the floor, using the algorithm and probability
 552 function described in Section 3.1 and Equation (3.6). Similar patterns can be observed, where
 553 highest concentration exists at the peak of the droplet and the lowest concentration is found
 554 in the corner of the droplet. We also observed that accumulating floor deposition patterns
 555 indeed do not show a coffee ring effect, confirming conclusions made from graphing flux from
 556 a fully absorbing floor.

557 **8. Conclusion.** Greater understanding of particle deposition in porous material resulting
 558 from the evaporation of impure fluids can help mitigate long-term contamination or clogging,
 559 optimizing membrane performance in various industrial applications, such as fabrics and other
 560 filtration systems. This study provides a comprehensive study and parameter analysis on
 561 particle behavior in pores with a 2D model that does not rely on a small aspect ratio. Vi-
 562 sualizations of particle concentration give insight to particle distribution throughout a fluid,
 563 as well as pore radius and averaged concentration evolution patterns over time. Results show
 564 that particle deposition must accumulate given the assumption that deposition is irreversible,
 565 whereas concentration evolution is not necessarily monotonically increasing. The 2D PDE
 566 model produces steady results with initial radii between 0.05 to 10, where smaller radii begin
 567 exhibiting a small aspect ratio and give way to the asymptotically-reduced 2D PDE model.
 568 The asymptotic model is more computationally efficient for small initial radius (< 0.1).

569 Furthermore, the PDE model is compared with a stochastic interpretation that originates
 570 from leveraging connections between the 2D scaled diffusion equation and the 2D Fokker-
 571 Planck equation. A new algorithm for a partially absorbing SDE boundary is proposed.
 572 While there are some discrepancies in the behaviors of the PDE and SDE models, there
 573 are noticeable similarities between the models that allow for both a macro- and micro-scale
 574 understanding of physical phenomena in a fluid-filled pore channel. In particular, the SDE
 575 model is simpler when exploring different wall geometries, altering boundary conditions, and
 576 adding variation to particle-specific behaviors.

577 Since the PDE 2D model allows us to accommodate curved surfaces, the last part of
 578 the study investigates the behavior of a parabolic fluid-air interface through modeling the
 579 evaporation and deposition in a droplet. Concentration of particles and flux are visually
 580 comparable, exhibiting similar patterns. The SDE model, scaled or unscaled, is easier to
 581 manipulate and account for complex boundary conditions.

582 **9. Future Work.** Throughout this paper, we assume that the particle-laden fluids are
 583 originally dilute. In each simulation, we terminate the model before the evaporating surface
 584 reaches small \hat{z} , at which particles become too condensed [18, 13]. The model also assumes that
 585 particles are non-interacting and have negligible volume. This could be corrected using multi-
 586 phase mixture models that deal with higher particle density by incorporating non-constant
 587 diffusion. The nonlinear diffusion equation would then be

$$588 \quad \frac{\partial \phi}{\partial t} = \nabla^2(D(\phi)\phi).$$

589 Utilizing the nonlinear diffusion equation and PDE-related numerical methods, we can both
 590 validate existing assumptions with constant diffusion and dilute regimes, and generalize initial
 591 conditions to non-dilute solutions.

592 Additionally, we only consider a 2D quarter of the pore channel symmetric along the \hat{x}
 593 and \hat{z} axes. A more realistic geometry would be a 3D circular cylinder; the axi-symmetric
 594 version was done in [14]. Other physical considerations include curved interfaces due to
 595 surface tension, making the height $\hat{H}(\hat{x}, \hat{t})$. Depending on the mixture and the material of
 596 the walls, the fluid may have inward or outward curved surfaces instead, forming menisci that

597 evolves over time. In our model, local concentration also has a strong correlation with the
 598 concentration in the whole solution. As fluid evaporates and particle concentration increases,
 599 local concentration near the wall becomes greater than C_{sat} and yields deposition. We may
 600 also want to consider coupling the particle concentration to fluid dynamics for convection in
 601 the bulk. Ultimately, there is still much to be explored and expanded upon as we aim for a
 602 more comprehensive and thorough framework for fluid-filter phenomena.

603 **Acknowledgments.** This article would not have been possible without the exceptional
 604 support of our faculty supervisor, Dr. Thomas Witelski, and our graduate student supervi-
 605 sor, Yuqing Dai. We give credit to the study group report written during the 37th Annual
 606 Workshop on Mathematical Problems in Industry (MPI) in 2021, published in Mathemat-
 607 ics in Industry Reports, for proposing the topics discussed in this paper and for laying the
 608 foundation for our research. We would also like to show our gratitude to Dr. Vasu Venkatesh-
 609 waran from W. L. Gore & Associates, a material science company, who gave an industrial
 610 perspective to our work. An additional acknowledgement goes to Dr. Jonathan Mattingly for
 611 providing insight to stochastic boundary conditions. Lastly, we are also immensely grateful
 612 to Dr. Heekyoung Hahn and Dr. Lenhard Ng, co-directors for the DMath program, for pro-
 613 viding us with this opportunity. Some support for our project was provided by Dr. Witelski's
 614 grant, NSF DMS 2008255.

Appendix A. Derivation of Moving Boundary Condition. Here we derive the form
 of a prescribed-flux moving boundary condition (with prescribed normal flux $J(x, t)$); this is
 needed on two boundaries of our model. Let $C(x, z, t)$ be particle concentration defined on
 the region $0 < x < L$, $0 < z < G(x, t)$, and evolving according to the diffusion equation

$$C_t = D(C_{xx} + C_{zz}).$$

615 Let $F(x, z, t) := z - G(x, t)$ be the level set function defining the moving (top) boundary as
 616 $F = 0$. Assume there is no flux out through the left ($x = 0$), right ($x = L$), and bottom
 617 ($z = 0$) boundaries. Define $M(t) := \int_0^L \int_0^{G(x,t)} C(x, z, t) dz dx$ to be the total mass of particles
 618 in the domain at time t . Then, there is only flux through the top ($z = G$) boundary, and we
 619 have

620 (A.1)
$$\frac{dM}{dt} = - \int_{F=0} J(x, t) ds = - \int_0^L J(x, t) |\nabla F| dx$$

621 because the line integral can be represented as a single integral with respect to x , where the
 622 arclength ds is given by $|\nabla F| dx$. From another perspective, the rate of change in mass can
 623 also be expressed as

624 (A.2)
$$\frac{dM}{dt} = \int_0^L \left(\int_0^{G(x,t)} \frac{\partial C}{\partial t} dz + C(x, G(x, t), t) \frac{\partial G}{\partial t} \right) dx$$

625 by the Leibniz integral rule. Using the diffusion equation then gives

626 (A.3)
$$\frac{dM}{dt} = D \int_0^L \int_0^{G(x,t)} \nabla \cdot \nabla C dz dx + \int_0^L C(x, G(x, t), t) \frac{\partial G}{\partial t} dx.$$

627 The double integral can be written as a line integral using the 2D Divergence Theorem,
 628 resulting in

$$629 \quad (A.4) \quad \frac{dM}{dt} = D \int_{\{F=0\}} \nabla C \cdot \frac{\nabla F}{|\nabla F|} ds - \int_0^L C \frac{\partial F}{\partial t} dx.$$

630 Again, rewriting the line integral gives

$$631 \quad \frac{dM}{dt} = D \int_0^L \nabla C \cdot \nabla F dx - \int_0^L C \frac{\partial F}{\partial t} dx.$$

632 Equating Equation A.1 and Equation A.4 gives

$$633 \quad D \nabla C \cdot \nabla F - C \frac{\partial F}{\partial t} = -|\nabla F| J$$

634 and finally, using $\nabla F = (-G_x, 1)$,

$$635 \quad (A.5) \quad DC_x G_x - DC_z - CG_t = \sqrt{1 + G_x^2} J$$

636 which is then applied to the top and right boundaries in Section 2.1.

637

REFERENCES

- 638 [1] C. BREWARD, F. B. PLANELLA, D. A. EDWARDS, K. KIRADJIEV, A. KOVACS, S. L. SMITH, D. RUM-
 639 SCHITZKI, P. SANAEL, Y. SUN, T. WITELSKI, AND M. ZYSKIN, Evaporation from porous media,
 640 pore-level analysis. 36th MPI workshop report, 2020.
- 641 [2] M. K. DAS, P. P. MUKHERJEE, AND K. MURALIDHAR, Porous media applications: biological systems,
 642 in Modeling Transport Phenomena in Porous Media with Applications, Springer, 2018, pp. 123–154.
- 643 [3] R. ERBAN AND S. J. CHAPMAN, Stochastic modelling of reaction–diffusion processes, vol. 60, Cambridge
 644 University Press, 2020.
- 645 [4] D. GROLIMUND, M. ELIMELECH, AND M. BORKOVEC, Aggregation and deposition kinetics of mobile
 646 colloidal particles in natural porous media, Colloids and Surfaces A: Physicochemical and Engineering
 647 Aspects, 191 (2001), pp. 179–188.
- 648 [5] E. HE, D. GUO, AND Z. LI, A widely applicable strategy for coffee-ring effect suppression and controllable
 649 deposition of nanoparticles utilizing ice drying, Advanced Materials Interfaces, 6 (2019), p. 1900446.
- 650 [6] J. HERZIG, D. LECLERC, AND P. L. GOFF, Flow of suspensions through porous media—application to
 651 deep filtration, Industrial & Engineering Chemistry, 62 (1970), pp. 8–35.
- 652 [7] C. N. KAPLAN AND L. MAHADEVAN, Evaporation-driven ring and film deposition from colloidal droplets,
 653 Journal of Fluid Mechanics, 781 (2015), p. R2, <https://doi.org/10.1017/jfm.2015.496>.
- 654 [8] P. LEHMANN, S. ASSOULINE, AND D. OR, Characteristic lengths affecting evaporative drying of porous
 655 media, Phys. Rev. E, 77 (2008), p. 056309, <https://doi.org/10.1103/PhysRevE.77.056309>.
- 656 [9] B. LEIMKUEHLER, A. SHARMA, AND M. V. TRET'YAKOV, Simplest random walk for approximating robin
 657 boundary value problems and ergodic limits of reflected diffusions, The Annals of Applied Probability,
 658 33 (2023), pp. 1904–1960.
- 659 [10] T. METZGER AND E. TSOTSAS, Influence of pore size distribution on drying kinetics: A simple capillary
 660 model, Drying Technology, 23 (2005), pp. 1797–1809, <https://doi.org/10.1080/07373930500209830>.
- 661 [11] G. A. PAVLIOTIS, Stochastic processes and applications: diffusion processes, the
 662 Fokker-Planck and Langevin equations, vol. 60, Springer, 2014.
- 663 [12] A. J. PELLEJ AND N. TUFENKJI, Effect of particle size and natural organic matter on the migration
 664 of nano-and microscale latex particles in saturated porous media, Journal of colloid and interface
 665 science, 321 (2008), pp. 74–83.

- 666 [13] A. F. ROUTH AND W. B. ZIMMERMAN, Distribution of particles during solvent evaporation from films,
667 Chemical Engineering Science, 59 (2004), pp. 2961–2968.
- 668 [14] P. SANAIE, C. BREWARD, M. ELLIS, S. HAN, B. HOLZER, H. JI, H. EL KAHZA, S. L. SMITH, S. PARSA,
669 H. REYNOLDS, J. TROY, T. WITELSKI, N. ZHANG, AND M. ZYSKIN, Evaporation and deposition in
670 porous media, Mathematics in Industry Reports, (2021).
- 671 [15] Y. SHI, C. ZHANG, R. LI, S. ZHUO, Y. JIN, L. SHI, S. HONG, J. CHANG, C. ONG, AND P. WANG, Solar
672 evaporator with controlled salt precipitation for zero liquid discharge desalination, Environmental
673 science & technology, 52 (2018), pp. 11822–11830.
- 674 [16] S. F. SHIMOBAYASHI, M. TSUDOME, AND T. KURIMURA, Suppression of the coffee-ring effect by
675 sugar-assisted depinning of contact line, Scientific reports, 8 (2018), p. 17769.
- 676 [17] J. M. STAUBER, S. K. WILSON, B. R. DUFFY, AND K. SEFIANE, On the lifetimes of evaporating droplets,
677 Journal of Fluid Mechanics, 744 (2014).
- 678 [18] T. YOO, B. CHUN, AND H. W. JUNG, Practical drying model for horizontal colloidal films in rapid
679 evaporation processes, Drying Technology, 40 (2022), pp. 516–526.